Nanoscale

PAPER

View Article Online
View Journal | View Issue

Cite this: *Nanoscale*, 2018, **10**, 21772

Detection of lymph node metastasis with near-infrared upconversion luminescent nanoprobes†

Shanshan Qiu,‡[a,b] Jianfeng Zeng,‡[a,b] Yi Hou,[c] Lei Chen,[a,b] Jianxian Ge,[a,b] Ling Wen,[b] Chunyan Liu,[c] Youjiu Zhang,[a,b] Ran Zhu*[a,b] and Mingyuan Gao*[a,b,c]

The detection of lymph node metastasis is of great importance for therapy planning and prognosis of cancers, but remains challenging in the clinic. In the current study, we report a tumor-specific imaging probe constructed with $NaGdF_4$:Yb,Tm,Ca@$NaLuF_4$ core@shell upconversion nanoparticles showing distinctive near infrared emission. The following studies revealed that the characteristic Tm dopant emission at 804 nm showed a penetration depth up to 7.7 mm through multi-layered mice skin tissues, substantially greater than emissions at 655 nm and 541 nm typically from the widely used Er dopant, which is apparently favorable for sensitive tumor diagnosis. The cell binding assay further revealed that the anti-HER2 antibodies covalently attached on the particle surface endowed the nanoprobe with excellent binding specificity in targeting HER2-positive cancer cells *in vitro*, which further enabled the detection of lymph node metastasis of breast cancer *in vivo* in mice. In addition, the pharmacokinetics of the resulting nanoprobes were intensively studied through both upconversion luminescence imaging and SPECT imaging for comparing with that of the mother particles. The results obtained through both approaches were well consistent and revealed that the surface conjugation of antibodies largely altered the pharmacokinetic behaviors and substantially prolonged the blood half-life of the underlying nanoparticles, which was never reported before.

Received 18th July 2018,
Accepted 1st November 2018

DOI: 10.1039/c8nr05811c

rsc.li/nanoscale

Introduction

Metastasis signifies not only the malignancy, but also the poor prognosis of cancers.[1,2] It is therefore taken as a key element in cancer staging systems such as the TNM staging system, where M represents metastasis which places a cancer in stage IV.[3,4] Typically, the circulating tumor cells acquire the ability to penetrate the walls of lymphatic or blood vessels, and then spread through the lymphatic or hematological system.[5–7] Lymphatic metastasis thus becomes one of the major causes of the high mortality rate of cancer patients. Therefore, precise detection of lymphatic metastasis is of great significance.

To date, lymph node (LN) biopsy has been considered as a gold standard for diagnosing lymphatic metastasis in many cancers, especially in breast cancer.[8,9] In order to obtain specimens of LNs for biopsy, blue dye, ^{99m}Tc-radiocolloid, and indocyanine green (ICG, a fluorescent dye) are practically used to map the sentinel lymph node (SLN) and guide the lymphadenectomy.[10–12] Although the value of these approaches has been proven by numerous clinical applications, a number of drawbacks remain. For instance, the blue dye is only visible in a shallow-located LN and it is also difficult to differentiate the SLN from the second or third LN due to the ready diffusion of the blue dye.[13,14] The ^{99m}Tc-radiocolloid can avoid missing a LN in deeper tissues, but is limited by it poor spatial resolution.[15–17] ICG is one of the near-infrared (NIR) fluorescent dyes currently approved by the FDA for SLN mapping, but the small molecular size leads to poor accumulation in the SLN.[18–21] Most importantly, all of these approaches cannot distinguish metastatic LNs from normal ones.

[a]*State Key Laboratory of Radiation Medicine and Protection, Soochow University, Suzhou, 215123, China. E-mail: gaomy@iccas.ac.cn, zhuran@suda.edu.cn*
[b]*Center for Molecular Imaging and Nuclear Medicine, School for Radiological and Interdisciplinary Sciences (RAD-X), Soochow University, Collaborative Innovation Center of Radiation Medicine of Jiangsu Higher Education Institutions, Suzhou 215123, China*
[c]*CAS Key laboratory of Colloid, Interface and Chemical Thermodynamics, Institute of Chemistry, Chinese Academy of Sciences, Beijing 100190, China*

† Electronic supplementary information (ESI) available: (1) Experimental details, (2) TEM, particle size histogram, and UCL spectrum of $NaGdF_4$:Yb,Er@$NaGdF_4$ nanoparticles, (3) colloidal stability and optical stability of PEGylated $NaGdF_4$:Yb,Tm,Ca@$NaLuF_4$ nanoparticles, (4) RE-staining results for cells incubated with the mother particles and NP-mAb probes, respectively, (5) quantitative UCL signals of the cells shown in Fig. 4, (6) pathological analysis of lymph nodes, (7) blood biodistribution profile of the ^{99m}Tc-labeled NP-mAb nanoprobes and mother nanoparticles recorded at different time points post-injection, (8) biodistribution of the ^{99m}Tc-labeled NP-mAb nanoprobes and mother nanoparticles in the main organs of mice recorded at 24 h postinjection. See DOI: 10.1039/c8nr05811c

‡ These authors contributed equally.

With the development of imaging technologies, different imaging modalities including computed tomography (CT), magnetic resonance imaging (MRI), and positron emission tomography (PET) have been applied for the pre-surgical evaluation of lymphatic metastasis with the aid of various types of imaging agents.[22–24] For example, Oh *et al.* developed a TaO_x nanoparticle-based contrast agent for the CT imaging of the SLN, while it cannot specifically image the metastatic LN due to the low binding specificity.[25] In addition, the damage caused by X-ray radiation to normal tissue is difficult to avoid. Although MRI is much safer, the relatively low sensitivity makes it challenging to detect micro-lymphatic metastasis.[26–28] To achieve highly sensitive imaging of metastatic LNs, Mumprecht *et al.* reported a PET probe constructed by radiolabeling the anti-LYVE-1 antibody with ^{124}I.[29] Although the lymphatic metastasis was efficiently and sensitively distinguished in mice, the low spatial resolution and high cost of the imaging facilities may limit its practical application.[30,31] Therefore, it is mandatory to develop innovative imaging approaches for detecting lymphatic metastasis with better safety profile and higher accuracy.

Owing to the fast data acquisition, high sensitivity, and excellent safety profile with no harmful radiation involved, optical imaging, particularly fluorescence imaging, has attracted a tremendous amount of attention.[26,32,33] The fluorescent probes for LN-targeted imaging can be generally divided into two categories: organic molecular probes and inorganic nanoparticulate probes. Organic molecular probes are usually fabricated by coupling various fluorophores with targeting molecules for acquiring imaging specificity. For example, Chen's group reported the NIR fluorescence imaging of lymphatic metastasis using tumor-specific antibodies labelled with a fluorescent dye.[34] Different from the organic dyes, fluorescent quantum dots (QDs) are characterized by size-tunable fluorescence and large specific area for hosting versatile targeting moieties. For instance, Cai's group reported a QD-luciferase conjugate for sensitive lymph node mapping.[35] However, the autofluorescence and penetration depth of visible light limit the clinical applications of conventional fluorescence imaging.[36–42] Fortunately, these drawbacks may in principle be overcome by upconversion luminescence (UCL) imaging that relies on upconversion nanoparticles (UCNPs), typically lanthanide-doped rare-earth nanoparticles. Because the upconversion luminescence is characterized by large anti-Stokes shifts, narrow emission peak, excellent photochemical stability, and especially minimized interference of autofluorescence background,[43–51] UCNPs are becoming highly favorable for tumor imaging diagnosis. For example, in our previous studies, $NaGdF_4$:Yb,Er nanoparticles were successfully used in detecting subcutaneous tumors smaller than 2 mm in diameter *in vivo* after covalent attachment of anti-tumor antibodies on the particle surface.[52] Furthermore, similarly structured nanoprobes with antibody or folic acid as the targeting moiety were also prepared for visualizing orthotopically transplanted tumors,[53] lymphatic micro-metastases,[54] and even primary colorectal cancers in mice.[55] Nevertheless, developing upconversion nanoprobes with large tissue penetration depth and high targeting specificity for lymphatic metastasis detection remains a challenging subject, but is very meaningful for clinical translation.

On the basis of our previous investigations, herein we report lymphatic metastasis imaging using $NaGdF_4$:Yb,Tm, Ca@$NaLuF_4$ core@shell upconversion nanoparticles with distinctive 804 nm emission that highlights the current imaging probe due to a much deeper tissue penetration of the emission light apart from the excitation light. In brief, anti-HER2 antibodies were covalently conjugated to the particle surface for detecting the HER2-positive breast cancer *in vivo*. Using a lymphatic metastasis mice model, we further showed that the nanoprobes could specifically image the metastatic lymph nodes in mice. Moreover, through the intrinsic UCL of the UCNPs and the radioactivity measurement *via* ^{99m}Tc attached on the particle surface, the pharmacokinetic behaviours of the resultant nanoprobes were systematically investigated.

Results and discussion

Preparation and characterization of hydrophobic $NaGdF_4$:Yb, Tm,Ca@$NaLuF_4$ core@shell nanoparticles

The emission position and intensity are the most important parameters for the sensitivity of upconversion luminescence imaging through UCNPs. Regarding the emission position, different from the extensively investigated Yb and Er co-doped rare-earth nanoparticles that emit both green and red lights,[52,53,55–59] Yb and Tm co-doped particles give rise to NIR emissions that are apparently more favorable for *in vivo* applications.[60] Regarding the emission intensity, constructing a proper core@shell structure has been demonstrated to be effective for enhancing the luminescence intensity of the core particles.[55,57] Alternatively, properly selecting a co-dopant can also enhance the luminescence of the UCNPs.[61–65] By taking all these factors into consideration, in the current study, $NaGdF_4$:Yb,Tm,Ca@$NaLuF_4$ nanoparticles showing enhanced NIR emission were designed and synthesized for detecting tumor lymphatic metastasis. In brief, the preparation of the hydrophobic $NaGdF_4$:Yb,Tm,Ca core and the following growth of the $NaLuF_4$ shell, to achieve $NaGdF_4$:Yb,Tm, Ca@$NaLuF_4$ core@shell nanoparticles, were carried out according to previous reports with slight modifications.[52,53,55,57,66] The transmission electron microscopy (TEM) images and size distribution profiles displayed in Fig. 1a–c show that both core and core@shell NPs are highly monodisperse with an average size of 29.3 ± 0.7 nm and 48.8 ± 1.4 nm, respectively, and apparently no secondary nucleation occurred during the shell coating process. In addition, under 980 nm laser excitation, the $NaGdF_4$:Yb,Tm,Ca core particles exhibited a distinct NIR emission centered at 804 nm which can be attributed to the transitions from the $^3H_4$ state to the $^3H_6$ state of Tm^{3+}. According to the emission intensity, the shell coating further increases the luminescence intensity of the core@shell particles by a factor of 3, as shown in Fig. 1d.

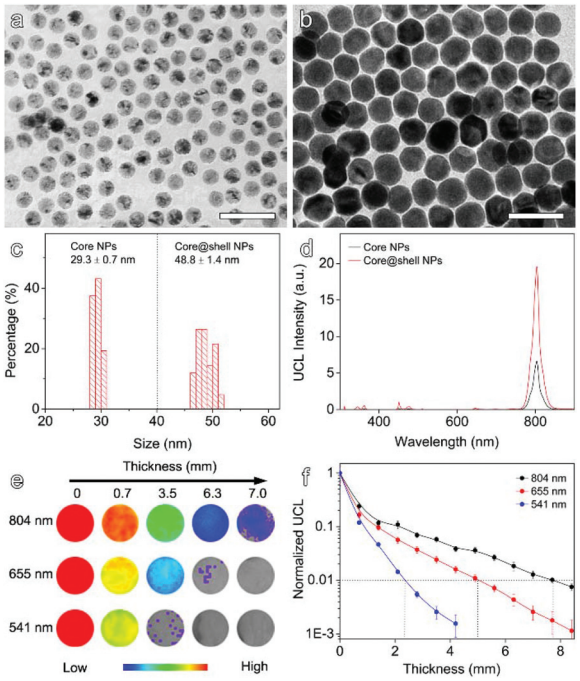

Fig. 1 TEM images of the hydrophobic $NaGdF_4$:Yb,Tm,Ca core (a) and $NaGdF_4$:Yb,Tm,Ca@$NaLuF_4$ core@shell nanoparticles (b), together with their corresponding size histograms (c), and upconversion luminescence spectra (recorded upon excitation at 980 nm) (d), UCL images (e) and intensities (f) of the upconversion emissions of 804 nm, 655 nm, and 541 nm after passing through skin tissues of different thicknesses, respectively (the scale bars embedded in frame a and b correspond to 100 nm).

To quantitatively show the improved penetration depth of the 804 nm emission, $NaGdF_4$:Yb,Er@$NaGdF_4$ particles simultaneously showing emissions at 655 and 541 nm were also prepared (Fig. S1†); then the ability of these emissions passing through folded mouse skins was determined. The results in Fig. 1e reveal that the 804 nm signal remains detectable, which is defined as 1% of the original emission intensity left, even when the $NaGdF_4$:Yb,Tm,Ca@$NaLuF_4$ nanoparticles were covered by folded mouse skins up to 7.7 mm thick. In remarkable contrast, both 541 nm and 655 nm emissions decrease more dramatically and become barely detectable when the tissue thickness is increased to 2.3 mm and 5.0 mm, respectively (Fig. 1f). Therefore, $NaGdF_4$:Yb,Tm,Ca@$NaLuF_4$ nanoparticles hold great potential for detecting human breast cancers, because benefiting from the near-infrared excitation the detection depth is remarkably higher than those of most near-infrared light-emitting materials.

Surface PEGylation of $NaGdF_4$:Yb,Tm,Ca@$NaLuF_4$ particles

The as-prepared $NaGdF_4$:Yb,Tm,Ca@$NaLuF_4$ core@shell NPs were hydrophobic since they were capped by oleic acid. To render the hydrophobic nanoparticles biocompatible, asymmetric polyethylene glycol (PEG) bearing a maleimide group at one end and a diphosphate group at the other end, denoted as mal-PEG-dp, was used to replace the oleate ligand since the diphosphate group possesses a much higher binding affinity to Lu^{3+}.[56,67] The resulting water-soluble nanoparticles are shown in Fig. 2a. Apparently, they barely show any change in particle size or size distribution profile throughout the ligand exchange process (Fig. 2b). The dynamic light scattering (DLS) results in Fig. 2c reveal that the PEGylated $NaGdF_4$:Yb,Tm,Ca@$NaLuF_4$ nanoparticles exhibit a narrow hydrodynamic size distribution in water with a single scattering peak located at 115 nm, which suggests that the mal-PEG-dp ligand could effectively replace the oleate ligand and no unwanted particle agglomerates were induced. More importantly, the NPs exhibited excellent colloidal stability in physiological medium (10% FBS) and no particle aggregates were detected over more than 7 days (Fig. S2†), which is essential for the particles to smoothly travel in the blood stream after being delivered through intravenous injection, whereas the excellent optical stability under physiological conditions is essentially meaningful for subsequent quantified *in vivo* imaging.

A good biocompatibility is one of the most important prerequisites for the *in vivo* application of any nanoprobe. Before further *in vivo* experiments, the cytotoxicity of the PEGylated $NaGdF_4$:Yb,Tm,Ca@$NaLuF_4$ nanoparticles was firstly evaluated through the MTT (3-(4,5-dimethylthiazol-2-yl)-2,5-diphenyltetrazolium bromide) cell proliferation assay on SKBR3 cells. As shown in Fig. 2d, the PEGylated $NaGdF_4$:Yb,Tm,Ca@$NaLuF_4$ nanoparticles present nearly no toxicity (cell survival rate higher than 80%) to SKBR3 cells below 5 mM which is one order of magnitude higher than the clinical dose for Gd-DTPA, *ca.*, 0.3 mM with respect to Gd^{3+}; therefore it is reasonable to believe that the $NaGdF_4$:Yb,Tm,Ca@$NaLuF_4$ nanoparticles prepared for the current study are safe as imaging agents, although the toxicity becomes dramatically enhanced if the Gd^{3+} concentration is above 10 mM.

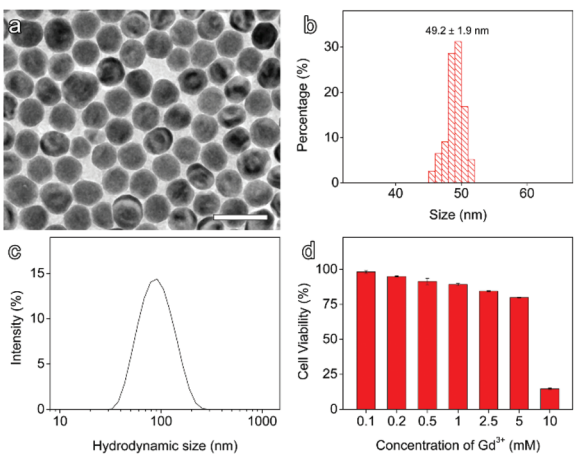

Fig. 2 TEM image (a), size histogram (b), and hydrodynamic size distribution profile (c) of the PEGylated $NaGdF_4$:Yb,Tm,Ca@$NaLuF_4$ particles, together with the cell viability of SKBR3 cells (d) recorded after being incubated with PEGylated $NaGdF_4$:Yb,Tm,Ca@$NaLuF_4$ nanoparticles with different Gd^{3+} concentrations (the scale bar embedded in frame a corresponds to 100 nm).

Specific probe for lymph node metastasis imaging

To actively target lymph node metastasis of breast cancer, the anti-HER2 monoclonal antibody (mAb) was conjugated to $NaGdF_4$:Yb,Tm,Ca@$NaLuF_4$ nanoparticles through a "click" reaction between the maleimide moiety of the PEG ligand on the particle surface and thiol residues from the partly reduced anti-HER2 mAb. The resulting conjugates (denoted as NP–mAb below) presented nearly unaltered optical emissions in comparison with the mother nanoparticles (Fig. 3a). Further DLS results shown in Fig. 3b reveal that the intensity-weighted hydrodynamic size of the nanoparticles is reasonably increased from 115 nm to 137 nm after the conjugation reaction. In addition, the particle surface zeta potential is also changed from 13.0 mV to −0.7 mV (Fig. S3†). The above results strongly support that the mAb molecules are effectively coupled onto the surface of UCNPs. In addition, the light scattering profile remains single-peaked after the conjugation reaction, suggesting that the conjugation reaction took place in a controlled manner.

To further validate the target-binding specificity, the NP–mAb conjugates were assessed through cell binding assays, in which an HER2 over-expressed human breast carcinoma cell line (SKBR3) and HER2 low-expressed cell lines (MCF7, MDA-MB 231, and HUVEC) were selectively used as the positive and negative controls, respectively. The binding affinity of NP–mAb to SKBR3 and its control cell lines was investigated with confocal microscopy. As shown in Fig. 4, the SKBR3 cells show intense UCL signals under 980 nm laser excitation after co-incubation with the NP–mAb nanoprobes for 2 h. In contrast, no evident upconversion signal is observed from SKBR3 cells after incubation with the mother nanoparticles or the control cell lines after incubation with the NP–mAb nanoprobes. Further quantitative analysis through the UCL signal revealed that the amount of nanoparticles in SKBR3 cells was more than 10-fold of that in the control cell lines after they were co-incubated with the nanoprobes under the same conditions (Fig. S4†). These results were also confirmed by staining the cells through the rare earth (RE) elements from UCNPs.[68] As shown in Fig. S5,† the SKBR3 cells labeled with the NP–mAb nanoprobes presented a green color much heavier than the controls, supporting that the NP–mAb probes possess a much stronger binding affinity to SKBR3 cells. In contrast, the binding affinity of either the mother NPs to HER2 positive tumor cells or the NP–mAb nanoprobes to HER-2 negative tumor cells was rather weak.

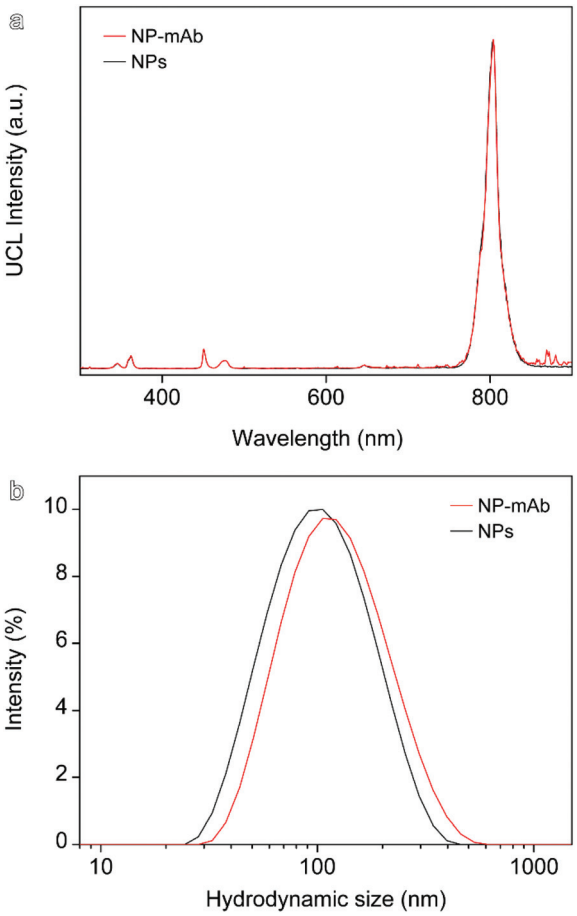

Fig. 3 The normalized upconversion luminescence spectra (a) together with the hydrodynamic size distribution profiles (b) of the mother particles and NP–mAb probes.

Lymphatic metastasis model

To show the *in vivo* imaging capability of the NP–mAb nanoprobes, a lymphatic metastasis mice model of HER2-positive breast cancer was established by injecting a SKBR3 cell suspension into the foot pads of female BALB/c nude mice. About 4 weeks after the inoculation of the tumor cells, the enlargement and hardening of popliteal lymph nodes became easily palpated. Then, the swollen lymph nodes were taken out for pathological analysis. The histopathological results shown in Fig. 5 demonstrate the successful metastasis of cancer cells to the popliteal lymph nodes. Statistically, about 70% of the mice were found with lymphatic metastasis 4 weeks after the foot pad inoculation of tumor cells. All animal procedures were performed in accordance with the Protocols of Laboratory Animals of Soochow University and the experiments were approved by the Animal Ethics Committee of Soochow University.

Imaging of lymphatic metastasis *in vivo*

The $NaGdF_4$:Yb,Tm,Ca@$NaLuF_4$ nanoparticles are characterized by their NIR excitation (980 nm) and emission (804 nm), and thus they are superior to those previously reported for *in vivo* applications. To explore the potential of the current nanoprobes in diagnosing metastatic lymph nodes, UCL imaging of mice with spherical hard lumps in their inner knee was performed. The NP–mAb nanoprobes obtained as mentioned above were intravenously injected with a dosage of 9 mg Gd per kg body weight, and the mother NPs were set as a negative control and used at the same dosage level according to Gd concentration. A set of upconversion fluorescence images taken at different time points postinjection is presented in

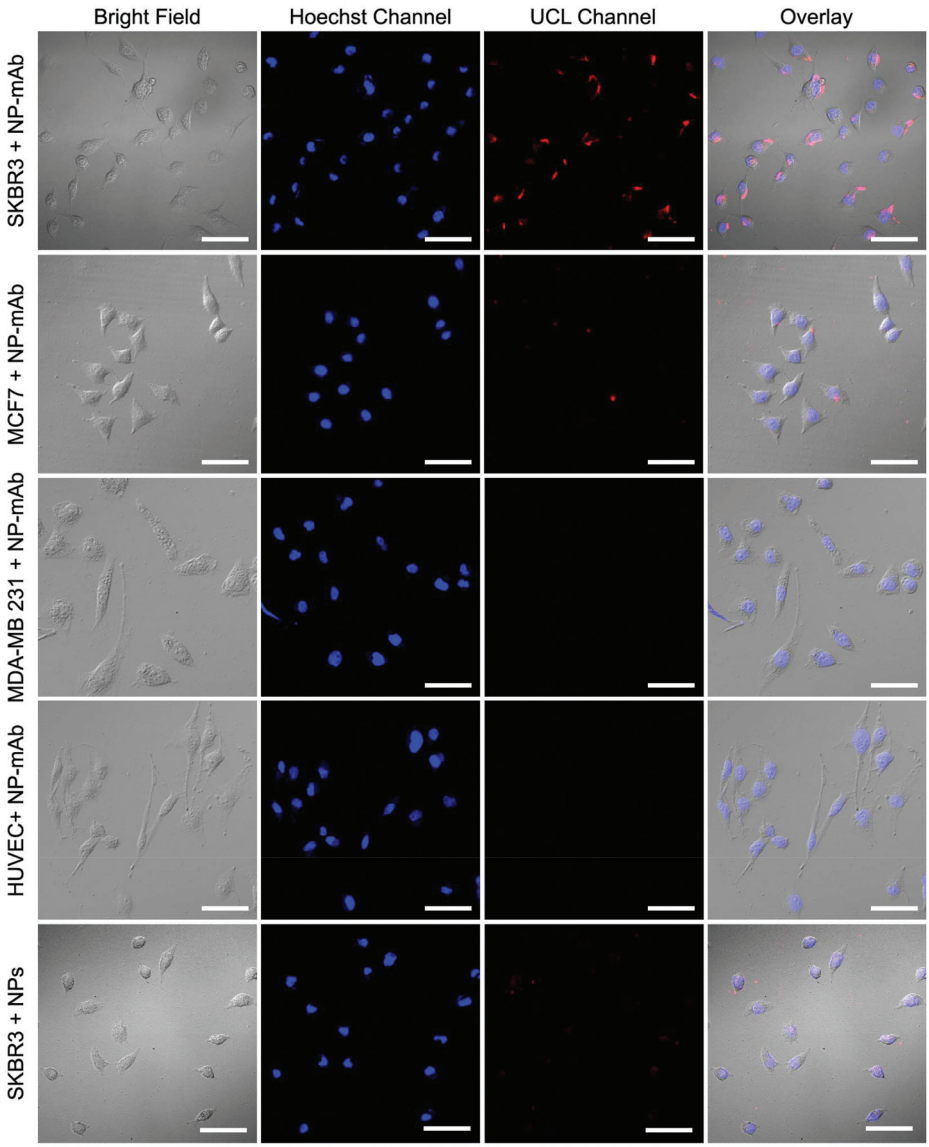

Fig. 4 Upconversion microscopy images of the HER2 over-expressed cell line (SKBR3) and HER2 low-expressed cell lines (MCF7, MDA-MB 231, and HUVEC) incubated with the NP–mAb conjugates and the mother nanoparticles, respectively. The bright field images (Bright Field), fluorescence images (Hoechst Channel, collected through a 420–520 nm window for the nuclei stained with Hoechst), and upconversion luminescence images (UCL Channel, collected through a 700–800 nm window) were captured and then merged together (Overlay) (the embedded scale bars correspond to 50 μm).

Fig. 6a. The upconversion luminescence signals of the lymph node site recorded before and after the injection of the NP–mAb nanoprobes and the mother particles, respectively, are plotted against postinjection time in Fig. 6b. It can be seen that a significant luminescence signal appears at the lymph node region 10 min after the delivery of the NP–mAb nanoprobes, and the signal intensity increases and reaches a maximum at 1 h postinjection, followed by a gradual decay upon prolonged observation. Different from the NP–mAb nanoprobes, the luminescence intensity of the mother UCNPs from the lymph node site reaches its maximum at 10 min postinjection. It then all the way goes down against time showing lowered intensities in comparison with those recorded from the NP–mAb nanoprobes, which indicates that the LN uptake of the mother particles is limited due to the lack of binding specificity. After the imaging experiments, the main organs including the heart, brain, lung, liver, spleen, kidney, stomach, large intestine, small intestine, and metastatic lymph node were harvested at 24 h postinjection and then subjected to *ex vivo* upconversion imaging (Fig. 6c) for assessing the biodistribution of the nanoprobes (Fig. 6d). Apparently, the liver and spleen uptake dominates the biodistribution for both NP–mAb nanoprobes and mother nanoparticles, which is typical of particulate probes due to the phagocytosis of the mononuclear phagocyte system (MPS).[69] However, the NP–mAb nanoprobes present lower liver and spleen uptake in comparison with the

mother nanoparticles. Moreover, the large intestine and small intestine exhibit a reversed tendency for showing upconversion signals. These results imply that the antibody conjugation may reduce the liver and spleen uptake of UCNPs, and meanwhile accelerate their elimination through the biliary pathway. In addition, the conjugation of the antibody also enhances the accumulation of UCNPs in the lung. Nevertheless, metastatic lymph nodes show no obvious difference between the NP–mAb group and the mother particle group due to the largely faded signal over 24 h of observation as shown in Fig. 6b.

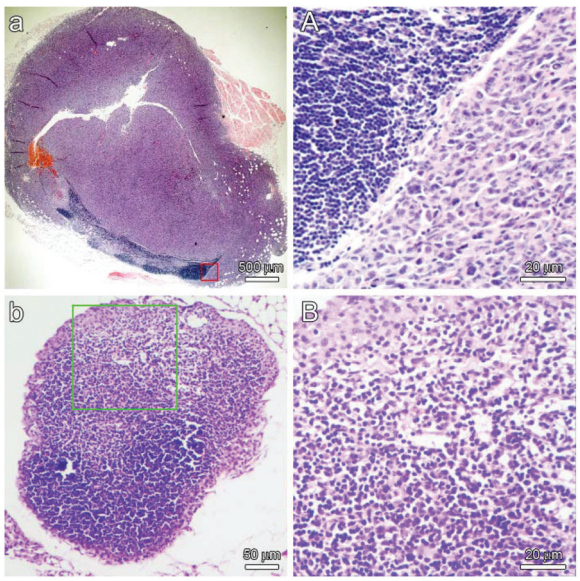

Fig. 5 Histopathological images of metastatic (a) and benign (b) lymph nodes together with the high magnification images (A, B) for showing the details of the regions enwrapped by red and green squares, respectively.

To further verify the specificity of the NP–mAb nanoprobes in targeting the lymphatic metastasis, nude mice bearing metastatic lymph nodes were intravenously injected with the NP–mAb nanoprobes or mother nanoparticles and then imaged under 980 nm excitation at 1.5 h postinjection, where the NP–mAb nanoprobes and mother nanoparticles exhibited the maximized difference as indicated in Fig. 6b. As shown in Fig. 7a and b, the NP–mAb nanoprobes present stronger upconversion signals at the lymph node region than the mother nanoparticles, which is well consistent with that captured at 1.5 h postinjection as shown in Fig. 6a. The main organs and tissues were immediately harvested right after capturing the images given in Fig. 7a and b and then photographed under 980 nm excitation *ex vivo*. As shown in Fig. 7c and d, the NP–mAb nanoprobes give rise to stronger upconversion luminescence from the lymph nodes than the corresponding mother particles. The quantified signals in Fig. 7e reveal that the upconversion signal of the NP–mAb nanoprobes is ~2 times that of the mother nanoparticles. To further confirm that the UCL signal is from the metastatic lymph nodes rather than from the benign ones, histological studies were conducted right after the upconversion luminescence imaging studies. The results given in Fig. S6† clearly support that the luminescent lymph nodes were the metastatic ones. In addition, the major organs and tissues were harvested and analyzed by ICP-MS for biodistribution study. As shown in Fig. S7,† the results are generally consistent with the biodistribution patterns obtained through upconversion imaging (Fig. 7e), in which the NP–mAb nanoprobes present lower MPS uptake and faster elimination through the biliary pathway.

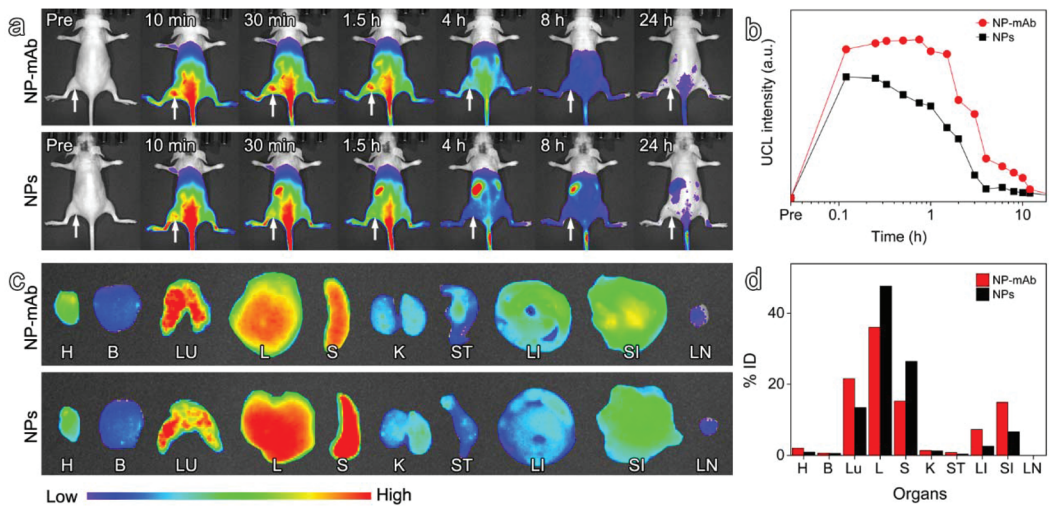

Fig. 6 (a) Upconversion luminescence images captured before and at different time points after the intravenous injection of the NP–mAb probes and mother NPs into nude mice bearing lymphatic metastasis, respectively, (b) temporal evolution of the integrated upconversion luminescence signal extracted from the lymph node site as indicated with white arrows in frame a, (c) *ex vivo* upconversion luminescence images of the main organs and lymph nodes captured at 24 h postinjection of the NP–mAb nanoprobes and mother NPs, respectively (H, heart; B, brain; L, liver; S, spleen; LU, lung; K, kidney; ST, stomach; LI, large intestine; SI, small intestine; LN, lymph node), (d) biodistribution of the NP–mAb nanoprobes and mother nanoparticles in the lymph nodes and main organs determined at 24 h postinjection by integrating the upconversion luminescence signals.

Pharmacokinetics of the NP–mAb nanoprobes

The pharmacokinetic behaviors closely related to the bioavailability of nanoparticles and possible undesirable side effects are more sophisticated for nanoparticle-based agents. Actually, through UCL the biodistributions of both the NP–mAb conjugates and the mother particles have already been revealed as shown in Fig. 6 and 7. In comparison with the results recorded at 24 h postinjection, due to much higher particle concentration in blood, the vascular organs including the liver, spleen, and lung exhibit remarkably stronger luminescence at 1.5 h postinjection. Nevertheless, the biodistribution patterns for both NP–mAb nanoprobes and mother nanoparticles do not change much against time. At both time points, *i.e.*, 24 h and 1.5 h, the NP–mAb nanoprobes show lower liver and spleen signals, and higher intestine and lung signals in comparison with the mother nanoparticles.

To provide more accurate pharmacokinetic information, both NP–mAb nanoprobes and mother nanoparticles were labeled with ^{99m}Tc through the chelating effect of the diphosphate group of the PEG ligand anchoring on the particle surface.[70] After the intravenous injection of the ^{99m}Tc-labeled NP–mAb nanoprobes or the mother nanoparticles (150 μL solution containing 180 μg Gd and 500 μCi ^{99m}Tc, corresponding to a dosage of 9 mg Gd and 25 mCi ^{99m}Tc per kg body weight), the nude mice were imaged using a small animal SEPCT/CT scanner. The images acquired at different time points postinjection, as given in Fig. 8a, indicate that both NP–mAb nanoprobes and mother nanoparticles mainly circulate in the blood stream at the initial stage as evidenced by the high signal from the heart. With prolonged observation, the NP–mAb nanoprobes and mother nanoparticles exhibit quite different pharmacokinetic behaviors. The mother nanoparticles were quickly cleared from the blood and then taken up by the liver and spleen within 1.5 h, while the NP–mAb nanoprobes show much slower liver and spleen accumulation and exhibit a strong signal in the heart even at 8 h postinjection. In addition, the radioactivity signal in the abdominal cavity is more intensive for the NP–mAb nanoprobes, especially at 24 h postinjection, supporting that the NP–mAb

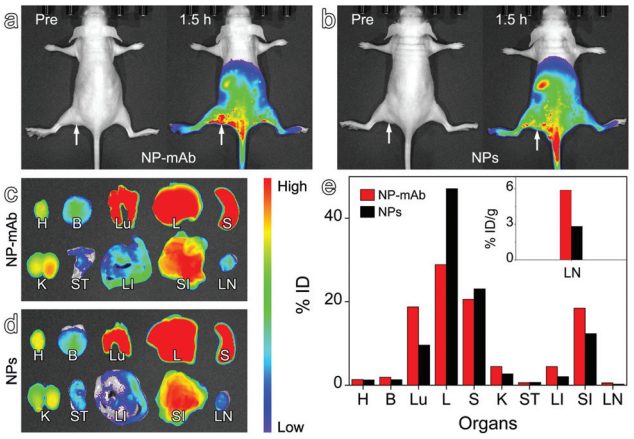

Fig. 7 Upconversion luminescence images captured before and at 1.5 h after intravenously delivering the NP–mAb nanoprobes (a) and mother nanoparticles (b), respectively, into nude mice bearing metastatic lymph nodes as indicated by the white arrows; *ex vivo* upconversion luminescence images of the main organs and lymph nodes captured right after acquiring the above images (c, d) (H, heart; B, brain; L, liver; S, spleen; LU, lung; K, kidney; ST, stomach; LI, large intestine; SI, small intestine; LN, lymph node), together with the quantified biodistribution profile (e) plotted according to the UCL signals in frames c and d.

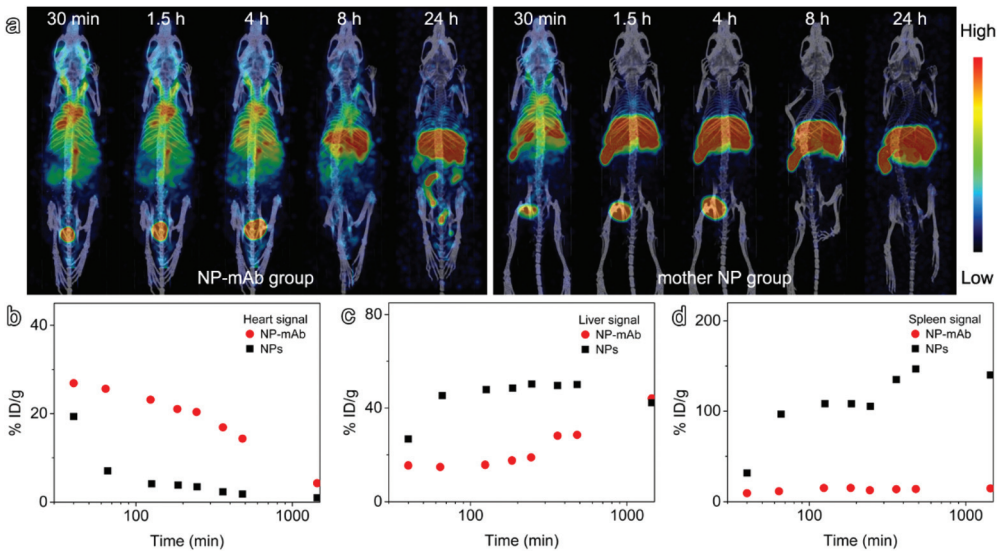

Fig. 8 SPECT/CT images (a) of nude mice intravenously injected with the ^{99m}Tc-labeled NP–mAb nanoprobes (left) and the ^{99m}Tc-labeled mother nanoparticles (right), respectively, together with the timely distribution of the NP–mAb nanoprobes and mother nanoparticles in different organs such as the heart (b), liver (c), and spleen (d).

nanoprobes are more readily excreted out of the body through the biliary elimination pathway.

The quantified SPECT results, acquired according to the volume of interest of the desired organs (Fig. 8b), reveal that the NP–mAb nanoprobes possess a much longer blood circulation time than the mother nanoparticles irrespective of the relatively large size of the UCNPs. At 8 h postinjection, the heart area holds 14.3%ID g^{-1} of NP–mAb nanoprobes, higher than half of the value (26.9%ID g^{-1}) recorded at 30 min postinjection, while the mother particles are almost cleared from the blood after 4 h of circulation. Further fitting the signal profile of blood with a one-compartment model resulted in half-lives ($t_{1/2}$) of 421 min and 41 min for the NP–mAb nanoprobes and mother nanoparticles, respectively (Fig. S8†). The underlying mechanism for the remarkably prolonged blood half-life of the NP–mAb conjugates remains unclear, but the long blood half-life is apparently favorable for effectively targeting the metastatic lymph nodes as the probes need to enter the lymphatic system from the hematological system after intravenous administration. In addition, the reduced uptake of UCNPs by the liver and spleen as a consequence of mAb conjugation, as shown in Fig. 8c and d, is also favorable for reducing possible side effects to these organs apart from being beneficial for long blood half-life.

After imaging at 24 h postinjection, the mice were sacrificed and the main organs were harvested and detected by using a gamma counter for biodistribution study. As shown in Fig. S9,† the summed uptakes by the liver and spleen are 42.6% and 70.2% for the NP–mAb nanoprobes and mother nanoparticles, respectively. In contrast, the radioactivity signal of the intestine (including both large intestine and small intestine) is much higher for the NP–mAb nanoprobes than that for the mother nanoparticles, *i.e.*, 15.0% *vs.* 0.9%. The excellent consistency between these results and those obtained through UCL (Fig. 6d) indicates that the current UCNPs may serve as a particle model for providing accurate information on the biodistribution of nanoparticles, due to the high tissue penetration depth and excellent optical stability of their NIR emission. In addition, in spite of a large number of nanoparticle–protein conjugates studied for various biomedical applications, the current study for the first time disclosed that antibody conjugation can suppress the uptake of nanoparticles by the MPS and accelerate the excretion through biliary elimination, even though it is at present not very clear why antibody conjugation can give rise to such an effect. Nevertheless, the current investigation suggests that antibody conjugation is helpful for achieving favorable pharmacokinetics.

Conclusions

In summary, biocompatible upconversion $NaGdF_4$:Yb,Tm, Ca@$NaLuF_4$ core@shell nanoparticles with enhanced NIR emission were prepared by replacing the oleate ligand of the as-prepared hydrophobic particles with the PEG ligand simultaneously bearing diphosphate and maleimide groups. The anti-HER2 monoclonal antibody was then covalently attached to the surface of the biocompatible particles for detecting lymphatic metastasis of HER2-positive breast cancer. The resulting NP–mAb nanoprobes presented excellent targeting ability and remarkable binding specificity to HER2-overexpressing cells *in vitro*, which enabled the successful detection of metastatic lymph nodes through upconversion luminescence *in vivo*. Most importantly, the pharmacokinetic studies through both upconversion luminescence and SPECT imaging suggest that antibody conjugation can prolong the blood half-life of UCNPs by evading the MPS uptake, which explains the outstanding performance of the resulting nanoprobes in diagnosing lymph node metastasis and therefore may also provide a valuable clue to tailor the pharmacokinetic behaviors of nanoprobes for versatile biomedical applications.

Conflicts of interest

There are no conflicts to declare.

Acknowledgements

This work was supported by the National Natural Science Foundation of China (81530057, 21503141, 81502758, and 81720108024), the National Key Research Program of China (2018YFA0208800), the China Postdoctoral Science Foundation (2015M570472, 2016T90489), and a project funded by the Priority Academic Program Development of Jiangsu Higher Education Institutions (PAPD).

Notes and references

1 S. D. Nathanson, *Cancer*, 2003, **98**, 413–423.
2 V. Pagliarulo, D. Hawes, F. H. Brands, S. Groshen, J. Cai, J. P. Stein, G. Lieskovsky, D. G. Skinner and R. J. Cote, *J. Clin. Oncol.*, 2006, **24**, 2735–2742.
3 S. B. Edge and C. C. Compton, *Ann. Surg. Oncol.*, 2010, **17**, 1471–1474.
4 B. Zee, *Cancer*, 2002, **94**, 1760–1769.
5 S. Y. Wong and R. O. Hynes, *Cell Cycle*, 2006, **5**, 812–817.
6 M. Banys, I. Gruber, N. Krawczyk, S. Becker, R. Kurth, D. Wallwiener, J. Jakubowska, J. Hoffmann, R. Rothmund and A. Staebler, *Breast Cancer Res. Treat.*, 2012, **131**, 801–808.
7 L. MF and E. T, *Int. J. Oncol.*, 2009, **34**, 881–895.
8 C. E. Cox, E. Dupont, G. F. Whitehead, M. D. Ebert, K. Nguyen, E. S. Peltz, D. Peckham, A. Cantor and D. S. Reintgen, *Breast J.*, 2015, **8**, 88–91.
9 K. M. Joyce, N. M. Mcinerney, C. W. Joyce, D. M. Jones, A. J. Hussey, P. Donnellan, M. J. Kerin, J. L. Kelly and P. J. Regan, *Ir. J. Med. Sci.*, 2015, **184**, 119–123.
10 J. How, W. H. Gotlieb, J. Z. Press, J. Abitbol, M. Pelmus, A. Ferenczy, S. Probst, R. Gotlieb, S. Brin and S. Lau, *Gynecol. Oncol.*, 2015, **137**, 436–442.

11 A. Buda, A. Papadia, I. Zapardiel, E. Vizza, F. Ghezzi, P. E. De, A. A. Lissoni, S. Imboden, M. D. Diestro and D. Verri, *Ann. Surg. Oncol.*, 2016, **255**, 1–7.
12 A. Papadia, I. Zapardiel, B. Bussi, F. Ghezzi, M. Ceccaroni, E. D. Ponti, F. Elisei, S. Imboden, B. D. Noval and M. L. Gasparri, *J. Cancer Res. Clin. Oncol.*, 2016, **143**, 475–480.
13 T. Hayashida, H. Jinno, M. Sakata, M. Takahashi, T. Onishi, H. Seki, T. Sato, T. Nakahara, N. Shigematsu and M. Mukai, *Eur. Surg. Res.*, 2010, **44**, 111–116.
14 E. A. O'Reilly, R. S. Prichard, A. D. Al, N. Aucharaz, G. Kelly, D. Evoy, J. Geraghty, J. Rothwell, A. O'Doherty and C. Quinn, *Ann. Surg.*, 2015, **262**, 243–248.
15 V. K. Sondak, D. W. King, J. S. Zager, S. Schneebaum, J. Kim, S. P. Leong, M. B. Faries, B. J. Averbook, S. R. Martinez and C. A. Puleo, *Ann. Surg. Oncol.*, 2013, **20**, 680–688.
16 J. L. Baker, M. Pu, C. A. Tokin, C. K. Hoh, D. R. Vera, K. Messer and A. M. Wallace, *Ann. Surg. Oncol.*, 2015, **22**, 40–45.
17 A. M. Marcinow, N. Hall, E. Byrum, T. N. Teknos, M. O. Old and A. Agrawal, *JAMA Otolaryngol. Head Neck Surg.*, 2013, **139**, 895–902.
18 W. Guo, L. Zhang, J. Ji, W. Gao, J. Liu and M. Tong, *Tumor Biol.*, 2014, **35**, 3073–3078.
19 A. Buda, B. Bussi, M. G. Di, L. P. Di, S. Palazzi, T. Grassi and R. Milani, *J. Minim. Invasive Gynecol.*, 2016, **23**, 265–269.
20 M. Plante, O. Touhami, X. B. Trinh, M. C. Renaud, A. Sebastianelli, K. Grondin and J. Gregoire, *Gynecol. Oncol.*, 2015, **137**, 443–447.
21 D. Samorani, T. Fogacci, I. Panzini, G. Frisoni, F. G. Accardi, M. Ricci, E. Fabbri, S. Nicoletti, L. Flenghi and E. Tamburini, *Eur. J. Surg. Oncol.*, 2014, **41**, 64–70.
22 G. Niu and X. Chen, *Theranostics*, 2015, **5**, 686–697.
23 C. Kollmann, *Eur. J. Radiol.*, 2007, **64**, 164–172.
24 S. Bipat, A. S. Glas, F. J. M. Slors, A. H. Zwinderman, P. M. M. Bossuyt and J. Stoker, *Radiology*, 2004, **232**, 773–783.
25 M. H. Oh, N. Lee, H. Kim, S. P. Park, Y. Piao, J. Lee, S. W. Jun, W. K. Moon, S. H. Choi and T. Hyeon, *J. Am. Chem. Soc.*, 2011, **133**, 5508–5515.
26 N. Kosaka, M. Bernardo, M. Mitsunaga, P. L. Choyke and H. Kobayashi, *Contrast Media Mol. Imaging*, 2012, **7**, 247–253.
27 H. J. Choi, S. H. Kim, S. S. Seo, S. Kang, S. Lee, J. Y. Kim, Y. H. Kim, J. S. Lee, H. H. Chung and J. H. Lee, *Am. J. Roentgenol.*, 2006, **187**, 538–543.
28 D. L. Thorek, D. Ulmert, N. F. Diop, M. E. Lupu, M. G. Doran, R. Huang, D. S. Abou, S. M. Larson and J. Grimm, *Nat. Commun.*, 2014, **5**, 3097.
29 V. Mumprecht, M. Honer, B. Vigl, S. T. Proulx, E. Trachsel, M. Kaspar, N. E. Banzigertobler, R. Schibli, D. Neri and M. Detmar, *Cancer Res.*, 2010, **70**, 8842–8851.
30 Z. Yang, R. Tian, J. Wu, Q. Fan, B. C. Yung, G. Niu, O. Jacobson, Z. Wang, G. Liu and G. Yu, *ACS Nano*, 2017, **11**, 4247–4255.
31 Y. Wang, L. Lang, P. Huang, Z. Wang, O. Jacobson, D. O. Kiesewetter, I. U. Ali, G. Teng, G. Niu and X. Chen, *Proc. Natl. Acad. Sci. U. S. A.*, 2015, **112**, 208–213.
32 K. Yuen, T. Miura, I. Sakai, A. Kiyosue and M. Yamashita, *J. Urol.*, 2015, **194**, 371–377.
33 H. Kobayashi, Y. Koyama, T. Barrett, Y. Hama, C. A. S. Regino, I. S. Shin, B. S. Jang, N. Le, H. P. Chang and P. L. Choyke, *ACS Nano*, 2007, **1**, 258–264.
34 X. Yang, Z. Wang, F. Zhang, G. Zhu, J. Song, G. J. Teng, G. Niu and X. Chen, *Theranostics*, 2017, **7**, 153–163.
35 A. Kamkaew, H. Sun, C. G. England, L. Cheng, Z. Liu and W. Cai, *Chem. Commun.*, 2016, **52**, 6997–7000.
36 T. Pons, E. Pic, N. Lequeux, E. Cassette, L. Bezdetnaya, F. Guillemin, F. Marchal and B. Dubertret, *ACS Nano*, 2010, **4**, 2531–2538.
37 E. Yaghini, H. D. Turner, M. A. Le, K. Suhling, I. Naasani and A. J. Macrobert, *Biomaterials*, 2016, **104**, 182–191.
38 G. François, B. Lina, L. Henri-Pierre, P. Emilie, R. Anne and M. Frédéric, *BMC Cancer*, 2008, **8**, 1–9.
39 Q. Miao, C. Xie, X. Zhen, Y. Lyu, H. Duan, X. Liu, J. Jokerst and K. Pu, *Nat. Biotechnol.*, 2017, **35**, 1102–1110.
40 Q. Miao and K. Pu, *Adv. Mater.*, 2018, **30**, 1801778.
41 C. Xie, X. Zhen, Q. Miao, Y. Lyu and K. Pu, *Adv. Mater.*, 2018, **30**, 1801331.
42 C. Xie, X. Zhen, Q. Lei, R. Ni and K. Pu, *Adv. Funct. Mater.*, 2017, **27**, 1605397.
43 L. Zeng, Y. Pan, R. Zou, J. Zhang, Y. Tian, Z. Teng, S. Wang, W. Ren, X. Xiao and J. Zhang, *Biomaterials*, 2016, **103**, 116–127.
44 Y. Li, Y. Gu, W. Yuan, T. Cao, K. Li, S. Yang, Z. Zhou and F. Li, *ACS Appl. Mater. Interfaces*, 2016, **8**, 19208–19216.
45 T. Zako, H. Nagata, N. Terada, A. Utsumi, M. Sakono, M. Yohda, H. Ueda, K. Soga and M. Maeda, *Biophys. Res. Commun.*, 2009, **381**, 54–58.
46 L. Cheng, *Angew. Chem., Int. Ed.*, 2011, **50**, 7385–7390.
47 Q. Han, Z. Dong, X. Tang, L. Wang, Z. Ju and W. Liu, *J. Mater. Chem. B*, 2016, **5**, 167–172.
48 N. Bogdan, F. Vetrone, G. A. Ozin and J. A. Capobianco, *Nano Lett.*, 2011, **11**, 835–840.
49 L. Q. Xiong, Z. G. Chen, M. X. Yu, F. Y. Li, C. Liu and C. H. Huang, *Biomaterials*, 2009, **30**, 5592–5600.
50 J. Zhou, Q. Liu, W. Feng, Y. Sun and F. Li, *Chem. Rev.*, 2015, **115**, 395–465.
51 X. Zou, M. Xu, W. Yuan, Q. Wang, Y. Shi, W. Feng and F. Li, *Chem. Commun.*, 2016, **52**, 13389–13392.
52 C. Liu, Z. Gao, J. Zeng, Y. Hou, F. Fang, Y. Li, R. Qiao, L. Shen, H. Lei, W. Yang and M. Gao, *ACS Nano*, 2013, **7**, 7227–7240.
53 Y. Hou, R. Qiao, F. Fang, X. Wang, C. Dong, K. Liu, C. Liu, Z. Liu, H. Lei, F. Wang and M. Gao, *ACS Nano*, 2013, **7**, 330–338.
54 R. Qiao, C. Liu, M. Liu, H. Hu, C. Liu, Y. Hou, K. Wu, Y. Lin, J. Liang and M. Gao, *ACS Nano*, 2015, **9**, 2120–2129.
55 C. Liu, Y. Qi, R. Qiao, Y. Hou, K. Chan, Z. Li, J. Huang, L. Jing, J. Du and M. Gao, *Nanoscale*, 2016, **8**, 12579–12587.

56 C. Wang, L. Cheng and Z. Liu, *Biomaterials*, 2011, **32**, 1110–1120.
57 R. Qiao, H. Qiao, Y. Zhang, Y. Wang, C. Chi, J. Tian, L. Zhang, F. Cao and M. Gao, *ACS Nano*, 2017, **11**, 1816–1825.
58 B. Shen, S. Cheng, Y. Gu, D. Ni, Y. Gao, Q. Su, W. Feng and F. Li, *Nanoscale*, 2017, **9**, 1964–1971.
59 M. Wang, C.-C. Mi, W.-X. Wang, C.-H. Liu, Y.-F. Wu, Z.-R. Xu, C.-B. Mao and S.-K. Xu, *ACS Nano*, 2009, **3**, 1580–1586.
60 M. K. Gnanasammandhan, N. M. Idris, A. Bansal, H. Kai and Z. Yong, *Nat. Protoc.*, 2016, **11**, 688–713.
61 Y. Li, Y. Gu, W. Yuan, T. Cao, K. Li, S. Yang, Z. Zhou and F. Li, *ACS Appl. Mater. Interfaces*, 2016, **8**, 19208–19216.
62 Z. Xiong, Y. Yang and Y. Wang, *RSC Adv.*, 2016, **6**, 75664–75668.
63 S. Liu, P. Zhang, D. Li, M. Lan, Z. Wang, W. Qin, D. Zhao and L. Wang, *J. Nanosci. Nanotechnol.*, 2016, **16**, 3883–3885.
64 L. Zhao, A. Kutikov, J. Shen, C. Duan, J. Song and G. Han, *Theranostics*, 2013, **3**, 249–257.
65 H. Jiang, X. Y. Zhao and K. S. Schanze, *Langmuir*, 2006, **22**, 5541–5543.
66 R. Qiao, C. Liu, M. Liu, H. Hu, C. Liu, Y. Hou, K. Wu, Y. Lin, J. Liang and M. Gao, *ACS Nano*, 2015, **9**, 2120–2129.
67 N. Bogdan, F. Vetrone, G. A. Ozin and J. A. Capobianco, *Nano Lett.*, 2011, **11**, 835–840.
68 J. Huang, Y. Hou, T. Ma, P. Zhang, Y. Li, C. Liu, B. Zhang, S. Qiu, J. Zeng and M. Gao, *Adv. Ther.*, 2018, **1**, 1800005.
69 M. X. Yu and J. Zheng, *ACS Nano*, 2015, **9**, 6655–6674.
70 Z. Gao, Y. Hou, J. Zeng, L. Chen, C. Liu, W. Yang and M. Gao, *Adv. Mater.*, 2017, **29**, 1701095.